Supplementary Information for

A tandem dye sensitized photoelectrochemical cells of mimicking photosynthesis for efficient H_2O_2 production without bias

Xin Zhang[a], Xinghua Guo[c], Degao Wang*[b,c,d]

[a.] School of Materials Science and Chemical Engineering, Ningbo University, Ningbo, 315211, China.

[b.] Qianwan Institute of CNITECH, Zhongchuang 1st Road, Zhongchuang Park, Qianwan New Area, Ningbo, Zhejiang 315336, China.Address here.

[c.] Ningbo Institute of Materials Technology and Engineering, Chinese Academy of Sciences (CAS), Ningbo, Zhejiang 315201, China.

[d.] Advanced Interdisciplinary Sciences Research (AIR) Center, Ningbo Institute of Materials Technology and Engineering, Chinese Academy of Sciences, Ningbo, China.

Correspondance: Wangdegao@nimte.ac.cn

Materials

All reagents are high purity reagents purchased through commercial sources, and have not been further purified before use. Aromatic amine, 2-Bromoethyl acetate (BEA), Disodium hydrogen phosphate (Na_2HPO_4), Sodium iodide (NaI), Sodium sulfate (Na_2SO_4), Sodium hydroxide (NaOH), 4,4'-Bipyridine (4,4'-bpy), Dichlororuthenium(II) cyclooctadiene polymer ($[RuCl_2(cod)]_n$), 2,2′-Bipyridine (2,2'-bpy), 2,2'-Bipyridine-6,6'-dicarboxylic acid (bda), 4,4′-Dibromo-2,2′-bipyridine (4,4'-dibromo-2,2'-bpy), Tetrakis(triphenylphosphine)palladium(0) ($Pd(PPh_3)_4$), Trimethylsilyl bromide (TMSBr), 4,4′-Bis(diethylphosphonate)-2,2′-bipyridine (4,4'-bis(Diethylphosphonate)-2,2'-bpy); Liquid reagents: Diethyl 2-bromoethylphosphonate (DEBEP), Hydrobromic acid (HBr), 2-Propanol (IPA), Triethylamine (Et_3N), Methanol (MeOH), Dichloromethane (DCM), o-Dichlorobenzene (o-DCB), Diethyl phosphite (DEP), Anhydrous toluene (anhydrous PhMe), Acetonitrile (CH_3CN), Ethanol (EtOH), Hydrochloric acid (HCl) were purchased from Shanghai Titan Scientific Co., Ltd.

Characterizations

^1H nuclear magnetic resonance (NMR) spectra were recorded on a Bruker 400 MHz or 500 MHz DCH cryoprobe spectrometer. For ^1H NMR spectra, chemical shifts are referenced to residual signals from the deuterated solvent. The crystalline structure of the samples was determined by powder X-ray diffraction (PXRD, D8 Advance) employing Cu Kα (λ = 0.154 nm) irradiation at 40 kV and 40 mA ranging from 2θ of 20° to 70° with 0.02° increment. Ultraviolet-visible (UV-vis) spectra were collected using a Varian Cary 50 Bio UV-vis spectrometer with quartz cuvettes (Hellma, 1 cm path length). The cross-sectional of glass was determined using a field-emission scanning electron microscope (SEM, Sigma 300, ZEISS, Germany) and a transmission electron microscope (TEM, Talos F200X G2, FEI, USA).

Atomic Layer Deposition (ALD)

NiO layer was deposited using Bis(N,N'-di-t-butylacetamidinato)nickel(II),

(99.999%-Ni) PURATREM) and deionized water as precursors via an instrument (GEMStar XT-D Bench-Top Atomic Layer Deposition). During the ALD process, the Ni precursor and deionized water reservoir was kept at 135 °C and room temperature, respectively, and the chamber temperature was set at 150 °C. The operation in one cycle was with a sequence of Ni precursor dose (0.5 s) holding for 20s, N_2 purge (40 s), H_2O dose (0.5 s) holding for 20s, N_2 purge (40 s). Then electrode was placed in the ALD chamber to deposit NiO layer.

Preparation of photocathodes

Standard precursor solutions of NiO were prepared by dissolv ing anhydrous $NiCl_2$ (1.0 g) and the P127 (1.0 g) into a mixture of Milli-Q water (3.0 g) and ethanol (6.0 g); The solution was left at rest for 3 days at 30 °C, and then centrifuged. Obtained supernatant solution was deposited on an FTO glass substrate by doctor blade method using mending tape (Scotch®) as a spacer, and dried at room tem perature. The dried film was heated to 450 °C at a ramping rate over 60 minutes in a muffle furnace, followed by calcination at this temperature for 30 minutes, obtained FTO|NiO. A dense NiO layer with varied cycle numbers was deposited onto FTO glass and nanoporous NiO substrates via ALD. The FTO|NiO|NiO glass slides were sequentially immersed in solutions of $NPhN_4$ (MeOH 5.0 mM), $ZrOCl_2$ (MeOH 3.0 mM), Por (DMF 5.0 mM), $ZrOCl_2$ (MeOH 3.0 mM) and PEV^{2+} (MeOH 5.0 mM) for 8, 2, 12, 2 and 3 hours, respectively, to yield the final dye-sensitized photocathode.

Preparation of photoanodes

The TiO_2 paste was doctor-bladed onto FTO glass substrates, with Scotch® masking tape used as spacers. The coated glass substrates were then air-dried at room temperature for 30 minutes. Subsequently, the dried glass was transferred into a muffle furnace, heated to 450 °C over a period of 60 min at a controlled heating rate, and calcined at this temperature for another 30 min, obtained FTO|TiO_2. A dense TiO_2 layer with 75 cycle was deposited onto FTO glass and nanoporous TiO_2 substrates via ALD. The FTO|TiO_2|TiO_2 glass slides were sequentially immersed in solutions of

$Ru(bda)(bpy)_2$ (MeOH 2.0 mM), and RuP (MeOH 2.0 mM) for 2 hours to yield the final dye-sensitized photocathode.

Measurement of H_2O_2

The amount of H_2O_2 was analyzed by iodometry. 1 mL of 0.1 M potassium hydrogen phthalate ($C_8H_5KO_4$) aqueous solution and 1 mL of 0.4 M potassium iodide (KI) aqueous solution were added to obtained solution, which was then kept for 30 min. H_2O_2 molecules react with iodine ions (I^-) under acidic conditions to generate triiodide ions (I_3^-), which have strong absorption near 350 nm. The absorbance of I_3^- at 350 nm is measured by ultraviolet spectrophotometer (UH5300), and then the amount of H_2O_2 generated by each reaction can be calculated.

Photoelectrochemical measurements

The photoelectrochemical measurements were performed on a CHI760E electrochemical workstation (CH Instruments). A custom H-type electrolytic cell was employed for all the measurements. The ORR toward hydrogen peroxide production at the photocathode was conducted under an O_2-saturated atmosphere. The electrolyte solution consisted of 0.1 M acetic acid/acetate buffer (pH 5.8) containing 0.5 M $NaClO_4$. A standard three-electrode configuration was adopted, where an Ag/AgCl electrode (saturated KCl) served as the reference electrode and a platinum electrode as the counter electrode. The light source was a 30 W LED lamp with an irradiance of 100 $mW \cdot cm^{-2}$ and a wavelength range of 410–750 nm, whose light intensity in the 410–750 nm region was comparable to that of one sun illumination. The electrochemical impedance spectra (EIS) were collected with the frequency range between 1×10^6 Hz to 1 Hz at an AC amplitude of 20 mV. LSV measurements were carried out at a scan rate of 0.05 $V \cdot s^{-1}$ over a potential range from 1 V to −1 V (vs. Ag/AgCl). CA measurements were recorded at a constant potential of −0.45 V (vs. Ag/AgCl). All potentials were converted to the RHE scale using the Eq. 1.

$$E(vs.RHE) = E(vs.Ag/AgCl) + 0.059 * pH + 0.197 \qquad \text{(Eq. 1)}$$

IPCE measurements were performed on a CIMPS-IPCE (Zahner) in 0.1 M acetic acid/acetate buffer (pH 5.8) containing 0.5 M $NaClO_4$. IPCE values were calculated from Eq. 2.

$$IPCE = \frac{1240 \times |J_{ph}|}{P_{mono} \times \lambda} \quad \text{(Eq. 2)}$$

In the tandem DSPEC system, the electrolyte solution consisted of 0.1 M acetic acid/acetate buffer (pH 5.8) containing 0.5 M $NaClO_4$. An unbiased two-electrode configuration was constructed, with a Nafion membrane inserted between the photocathode and photoanode. The photoanode chamber of the H-type cell was degassed with argon for 30 min and then sealed with vacuum sealant. AQE and SCC measurements were performed on a CIMPS-IPCE instrument (Zahner). For AQE tests, LED monochromatic light at wavelengths of 427 nm, 450 nm, 485 nm, 514 nm, and 566 nm was selected. For SCC efficiency measurements, a 300 W xenon lamp equipped with an AM 1.5G filter was used as the light source, and the light intensity was calibrated to 100 $mW \cdot cm^{-2}$ (1 sun). The amount of O_2 generated during water oxidation was monitored at the photoanode using a Clark-type oxygen sensor (Unisense Ox-N needle-type microsensor). The calibration curve was established by deoxygenation and oxygenation processes. Before the formal test, the dissolved oxygen content in the solution was stabilized for 25 minutes to ensure no air leakage.

The AQE values were calculated according to Eq. 3, and the SCC values were calculated according to Eq. 4.

$$AQE\ (\%) = \frac{m \times n \times N_A \times h \times c}{light\ intensity\ (mW \cdot cm^{-2}) \times illumination\ area\ (cm^2) \times t\ (s) \times \lambda} \quad \text{(Eq. 3)}$$

where m is the number of electrons transferred per product molecule. n is the amount of generated product (mol). N_A is the Avogadro number (6.02×10^{23}). h is the Planck constant (6.626×10^{-34} J·s), c is the speed of light (3.0×10^8 $m \cdot s^{-1}$), and λ is the wavelength of light. The illumination area was 1 cm^2.

$$SCC\ (\%) = \frac{\Delta G\ (J \cdot mol^{-1}) \times n\ (mol)}{light\ intensity\ (mW \cdot cm^{-2}) \times illumination\ area\ (cm^2) \times t\ (s)} \quad \text{(Eq. 4)}$$

where ΔG (H_2O_2) = 117 000 J·mol^{-1} and ΔG (O_2) = 475 000 J·mol^{-1} represent the Gibbs free energy changes for H_2O_2 and O_2 generation. The light intensity was 100 mW·cm^{-2}, the irradiated area was 1 cm^2, and the reaction time was 10800 s.

Details for *in-situ* DFTIRS measurement

In-situ diffuse reflectance infrared Fourier transform spectroscopy (DRIFTS) measurements were conducted using a Nicolet iS50 FT-IR spectrometer (Thermo Fisher Scientific, USA). Specifically, the photocathode was loaded into an *in-situ* infrared cell within the measurement chamber. Prior to data collection, the reaction cell was degassed under a controlled oxygen flow for 30 min to eliminate residual gases. A baseline spectrum was first acquired at room temperature as the reference. Subsequently, the LED lamp was used to irradiate the cell through the reactor window. *In situ* diffuse reflectance infrared Fourier transform spectroscopy (DRIFTS) measurements were first recorded at a constant potential of −0.45 V (vs. Ag/AgCl) at predetermined time intervals. After that, fresh samples were loaded, and *in-situ* DRIFTS measurements were performed over a potential range of −0.05 to 0.85 V (vs. Ag/AgCl) at different applied potentials.

Details for *in-situ* Raman measurement

In-situ Raman spectra were acquired using a LabRAM HR Evolution confocal Raman spectrometer (HORIBA Scientific). A 532 nm argon-ion laser served as the excitation source for Raman measurements. In situ Raman experiments were conducted in a custom-designed electrolysis cell, where NiO|–$NPhN_4$–Por–PEV^{2+} acted as the working electrode, a platinum plate was employed as the counter electrode, and a saturated KCl Ag/AgCl electrode was utilized as the reference electrode. Potentiostatic electrolysis tests at various applied potentials were performed in 0.1 M acetic acid/acetate buffer at pH 5.8 in 0.5 M $NaClO_4$.

Synthesis of $NPhN_4$

The $NPhN_4$ was synthesized following the reported method.[1] 0.05 mol aromatic amine was mixed with 0.21 mol 2-bromoethyl acetate, 0.25 mol disodium hydrogen phosphate and 0.05 mol NaI in 125 ml CH_3CN, heated and refluxed under argon protection for 12 h. after reaching room temperature, the mixture was concentrated in vacuum, and then water was added. Ethyl acetate was used to extract crude products from aqueous phase. The combined organic layers were washed with brine, dried with Na_2SO_4 and filtered. The product 1,4-bis (dimethyl azanediyldiacetate) benzene was obtained after removing the solvent under vacuum.

Ethanol solution (500 ml) of NaOH (0.25 mol) was added to the ethanol solution (100 ml) of 1,4-bis (dimethyl azanediyldiacetate) benzene synthesized above. The reaction mixture was heated to 60℃ and stirred at the same temperature for 4 h. after cooling to room temperature, the solid 1,4-bis (azadiacetate) benzene was obtained by filtration Then dissolve the solid in water and adjust the pH of the suspension to 1 with 37% HCl. The final product nphn4 was obtained by precipitation, filtration and vacuum drying. ^{1}H NMR (400 MHz, MeOD) δ 3.89 (s, 8H), 2.27 (s, 12H).

Synthesis of $[PEV\text{-}H][Br]_2$

The $[PEV\text{-}H][Br]_2$ was synthesized following the reported method.[2] Compound $[PEV\text{-}H][Br]_2$ was synthesized, following previously reported procedures, by an alkylation reaction between 4,4' bipyridine (250 mg, 1.6 mmol) and an excess of diethyl 2-bromoethylphosphonate (1.96 g, 8 mmol) under reflux conditions for 72 h in a H2O:CH3CN mixture (1:4 mL). After the reaction mixture cooled down (298 K), concentrated hydrobromic acid (48% v/v, 5 mL) was added and heated for 24 h, at reflux temperature. Then, the solution was concentrated to one half of its initial volume and 2-propanol (20 mL) was added dropwise; stirred in an ice bath for one hour and filtered off. The yellow crystalline product was washed with cold 2-propanol and air dried. Yield 82%.

Synthesis of $Ru(bda)(bpy)_2$

The Ru(bda)(bpy)$_2$ was synthesized following the reported method.[3] This complex was synthesized by a modified method reported in literature.3 A mixture of 2,2'-bipyridine-6,6'-dicarboxylic acid (bda) (488 mg, 2.0 mmol), Ru(DMSO)4Cl2 (968 mg, 2.0 mmol), and Et3N (1.6 mL) was refluxed in methanol (20 mL) for 4 h. After cooling to room temperature, the formed precipitate was filtered and washed with acetone and ether to get a reddish-brown powder of Ru(bda)(DMSO)2Cl2.

A 40 mL methanol solution containing Ru(bda)(DMSO)2Cl2 (500 mg, 1.0 mM) and 4,4'-bipyridine (4,4′-bpy 468 mg, 3.0 mmol) was refluxed for 4 h. The solvent was removed under reduced pressure, the residue was purified by silica gel chromatography with dichloromethane-methanol (20:1 to 1:1, V:V) as the eluent. Complex was obtained as a dark red solid. Yield: 371 mg (50%) ^{1}H NMR (400 MHz, DMSO) δ 8.76 (d, J = 7.5 Hz, 1H), 8.67 (d, J = 5.3 Hz, 2H), 7.99 – 7.83 (m, 4H), 7.70 (t, J = 6.8 Hz, 4H).

Synthesis of RuP

The RuP was synthesized following the reported method.[4] Dichlororuthenium(II) cyclooctadiene polymer (11.2 g, 40 mmol) and 2,2′-bipyridine (12.5 g, 80 mmol) were suspended in odichlorobenzene (100 mL). The reaction was heated to 190 °C under argon for 2 h. The mixture was allowed to cool, and a dark solid precipitated, which was filtered and washed with diethyl ether. This product was used without further purification. Yield: 17.9 g (92%).

4,4′-Bis(diethylphosphonate)-2,2′-bipyridine. Using Schlenk techniques to prevent air and moisture from entering the reaction vessel, diethyl phosphite (2.6 g, 20 mmol), 4,4′-dibromo-2,2′-bipyridine, (2.8 g, 8.8 mmol), and tetrakis(triphenylphosphine)palladium(0) (0.946 g, 0.819 mmol) were added to a flask under argon. Anhydrous toluene (86 mL) and triethylamine (2.6 mL) were then added, and the reaction was heated to 110 °C for 4 h. The reaction mixture was filtered hot, and the toluene was removed under vacuum. Recrystallization of the resulting residue from refluxing hexanes gave light-yellow needles of pure 4,4′-bis(diethylphosphonate)-2,2′-bipyridine. Yield: 1.95 g (51%). ^{1}H NMR (400 MHz, $CDCl_3$) δ 8.87 (t, J = 5.1 Hz,

2H), 8.81 (dd, J = 14.1, 1.3 Hz, 2H), 7.76 (ddd, J = 13.0, 4.8, 1.3 Hz, 2H), 4.34 – 4.12 (m, 8H), 1.39 (t, J = 7.1 Hz, 12H).

A solution of the ligand 4,4′-bis(diethylphosphonate)-2,2′-bipyridine (1.03 mmol) and cis-[$Ru(bpy)_2Cl_2$] in absolute EtOH (30 mL) was added to a Teflon vessel and heated in a microwave. The temperature was ramped to 150 °C over 5 min and then held at 150 °C for 20 min. After cooling to room temperature, EtOH was removed.

Hydrolysis. The isolated $[Ru(bpy)_2(4,4'\text{-}(CH_2PO_3H_2)_2bpy)]^{2+}$ complexes were hydrolyzed after isolation without any prior purification. $[Ru(bpy)_2(4,4'\text{-}(CH_2PO_3H_2)_2bpy)]^{2+}$ (0.50 mmol) was dissolved in 30 mL of anhydrous CH_3CN under an argon atmosphere. Trimethylsilyl bromide (1.02 equiv per−OEt group) was then added, and the reaction was heated at 70 °C for 48 h or until completion (as assessed by ^1H NMR of an aliquot of the reaction mixture). After cooling the reaction to room temperature, anhydrous MeOH (1.0 mL) was added and an orange solid precipitated from the reaction. The orange solid was filtered and washed with cool CH_3CN and Et_2O. Yield: 80%. ^1H NMR (400 MHz, D_2O) δ 8.66 (d, J = 12.7 Hz, 2H), 8.43 (d, J = 8.3 Hz, 4H), 7.95 (t, J = 7.6 Hz, 4H), 7.82 (dd, J = 5.8, 3.3 Hz, 2H), 7.69 (dd, J = 9.5, 5.6 Hz, 4H), 7.46 (dd, J = 11.5, 5.8 Hz, 2H), 7.27 (t, J = 6.7 Hz, 4H).

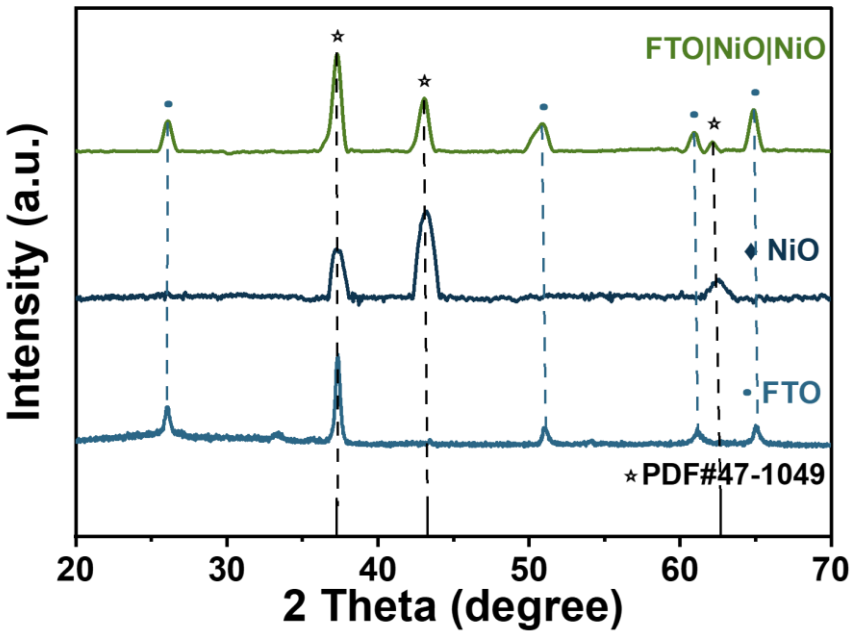

Fig. S1 PXRD patterns FTO, NiO, FTO|NiO|NiO.

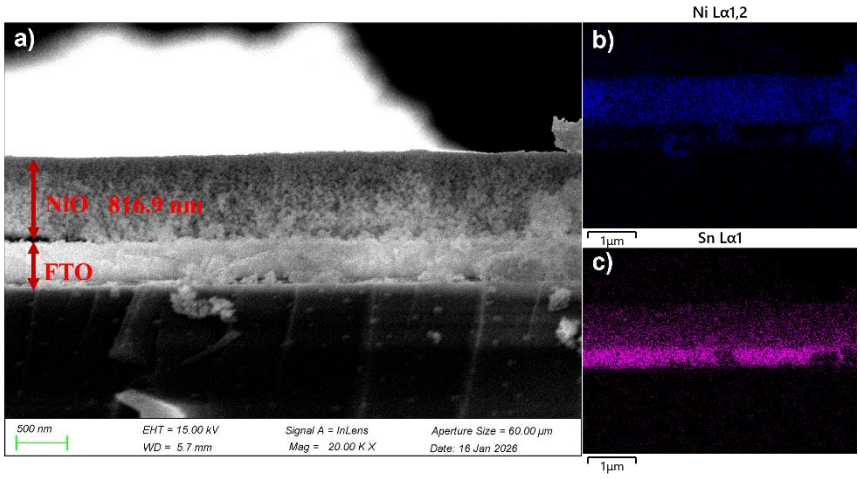

Fig. S2 Cross-sectional SEM images. a) Cross-sectional SEM images for FTO|NiO. EDS images for b) Ni, c) Sn.

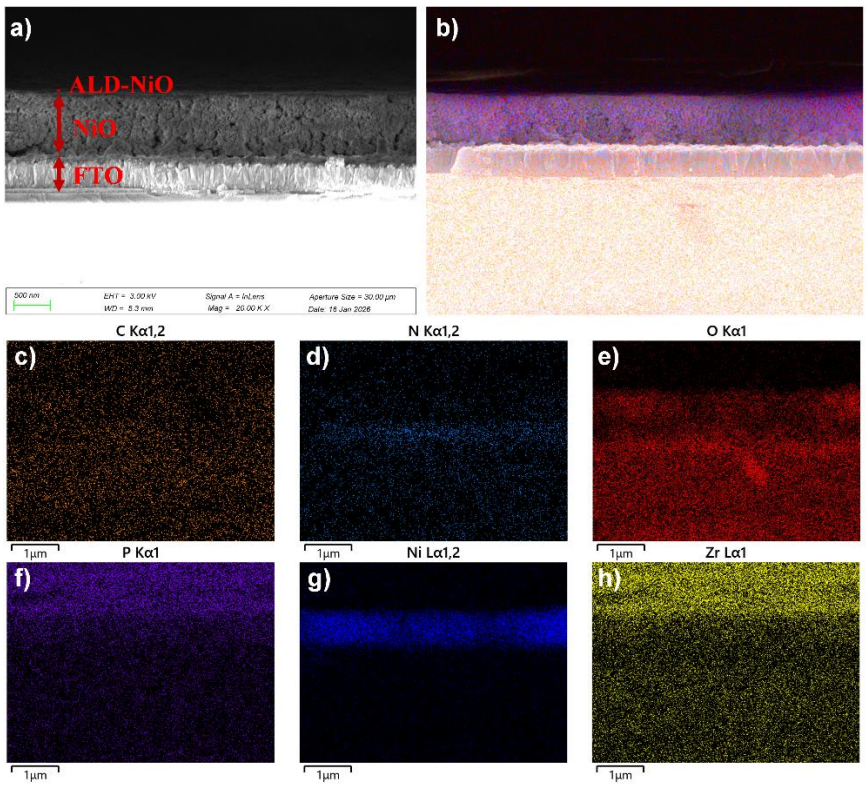

Fig. S3 Cross-sectional SEM images. a) Cross-sectional SEM images for FTO|NiO|NiO. b) EDS Elemental Mapping Images, c) C, d) N, e) O, f) P, g) Ni, and h) Zr.

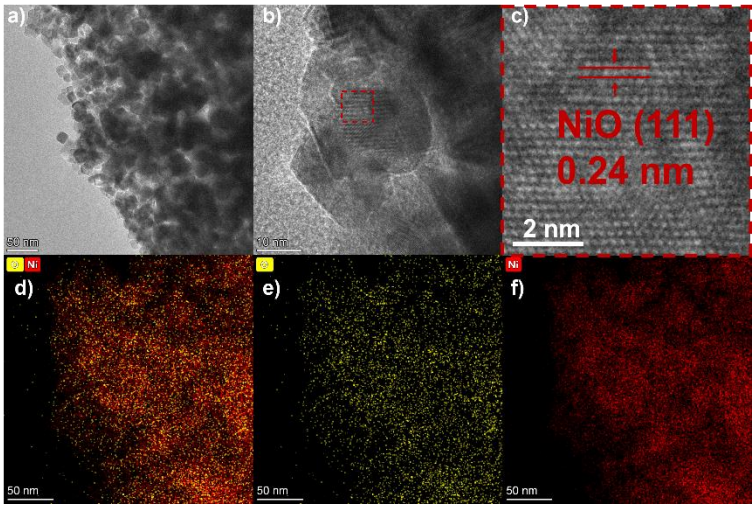

Fig. S4 TEM images of a-c) FTO|NiO|NiO with NiO deposited at 3 cycles. d) EDS Elemental Mapping Images, e) O, f) Ni.

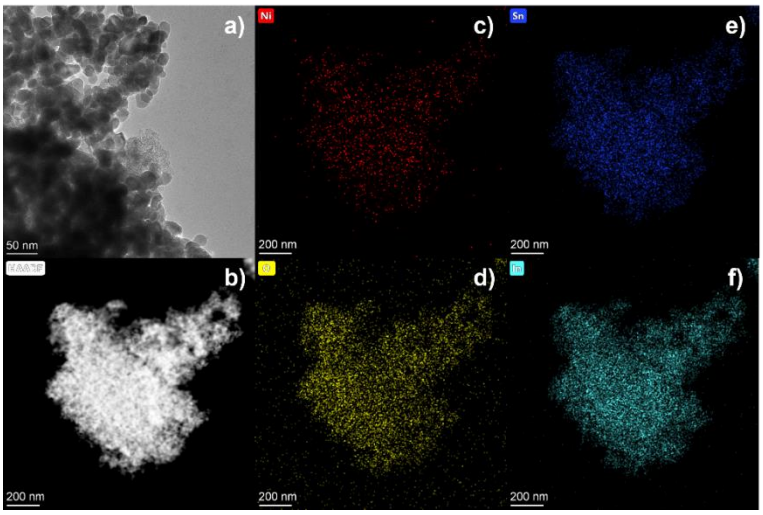

Fig. S5 TEM images of a) FTO|ITO|NiO with NiO deposited at 3 cycles. b) HAADF-STEM image. EDS Elemental Mapping Images, c) Ni, d) O, e) Sn, and f) In.

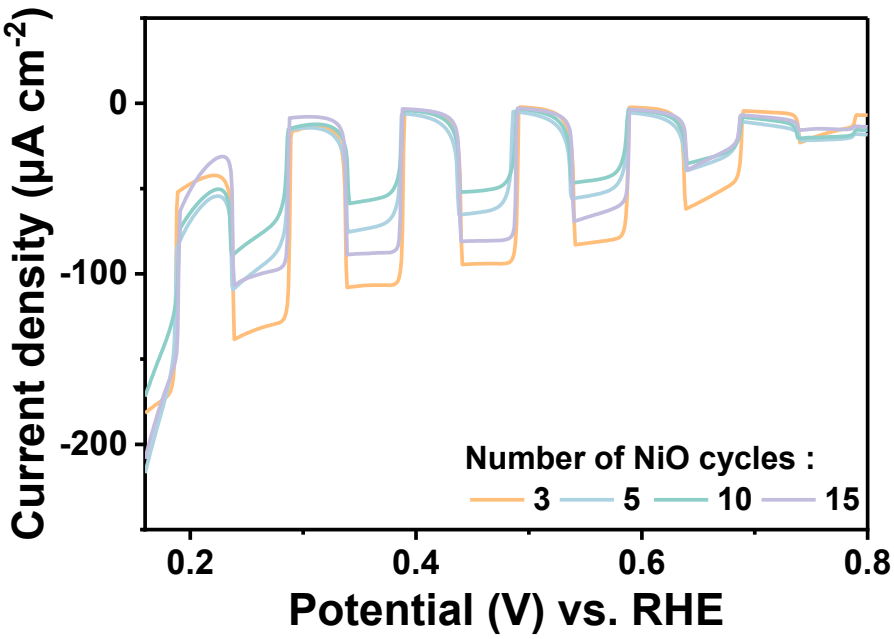

Fig. S6 LSV curves with chopped light. NiO|–$NPhN_4$–Por–PEV^{2+} hotocathodes with various ALD deposition cycles of NiO (scan rate: 50 $mV \cdot s^{-1}$) were conducted in 0.1 M acetic acid/acetate buffer at pH 5.8 in 0.5 M $NaClO_4$.

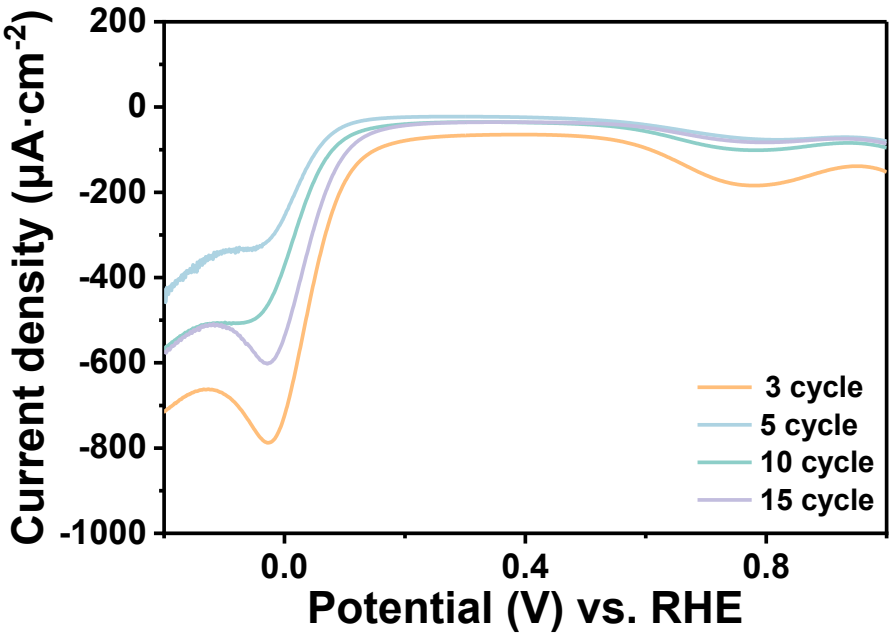

Fig. S7 LSV plots. NiO|–NPhN$_4$–Por–PEV^{2+} photocathodes with various ALD deposition cycles of NiO (scan rate: 50 mV·s^{-1}) were conducted in 0.1 M acetic acid/acetate buffer at pH 5.8 in 0.5 M NaClO$_4$.

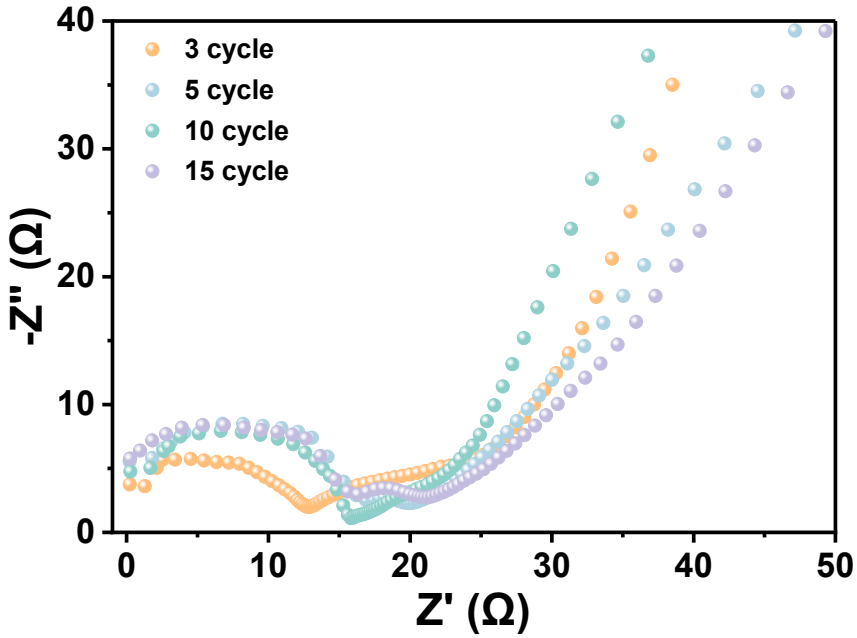

Fig. S8 Electrochemical impedance spectroscopy. Nyquist plots (scatter) for NiO|–NPhN$_4$–Por–PEV^{2+} photocathode with various ALD deposition cycles of NiO.

The charge transfer resistance of NiO films deposited via ALD with varying cycle numbers exerts a pronounced influence on the photocurrent density of the photoelectrode. Specifically, the photocathode with NiO deposited at 3 cycles delivers the maximum photocurrent, which is attributed to its optimal light absorption capability and charge transfer resistance characteristics.

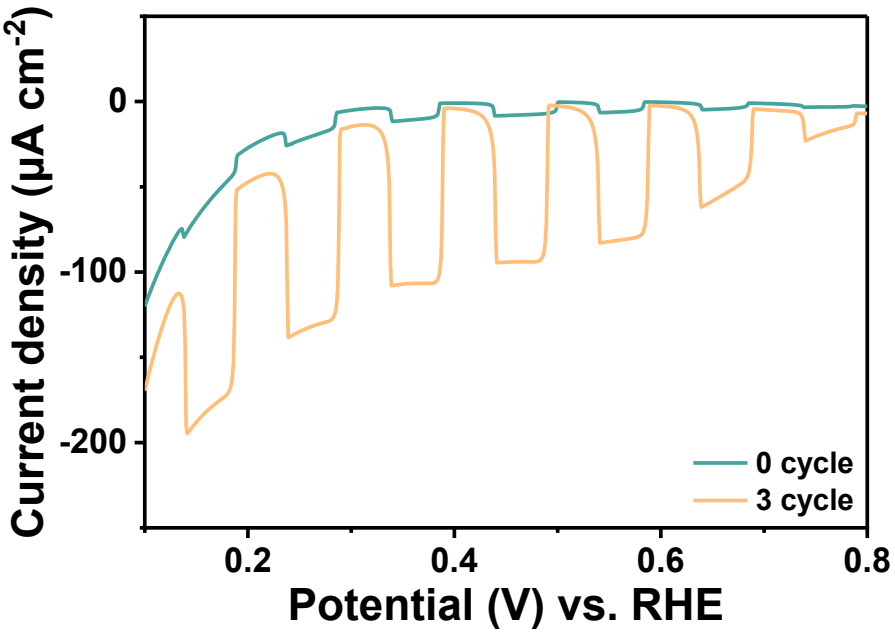

Fig. S9 LSV curves with chopped light. NiO|–NPhN$_4$–Por–PEV^{2+} photocathodes with or without NiO deposited at 3 cycles (scan rate: 50 mV·s^{-1}) were conducted in 0.1 M acetic acid/acetate buffer at pH 5.8 in 0.5 M NaClO$_4$.

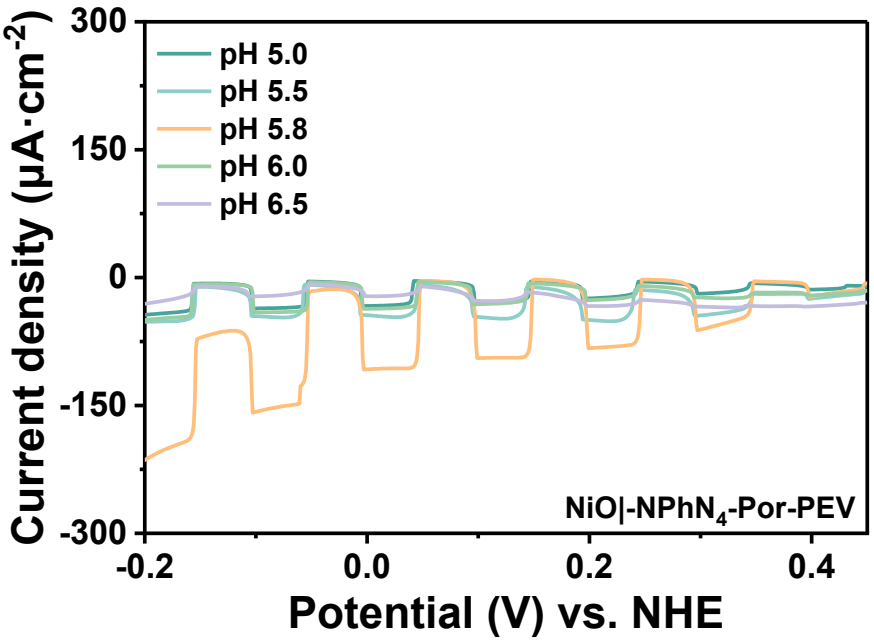

Fig. S10 PEC performance of the photocathode in varied pH conditions. LSV measurements of NiO|–NPhN$_4$–Por–PEV^{2+} in the electrolyte with pH varied from 5.0 to 6.5 under chopped light.

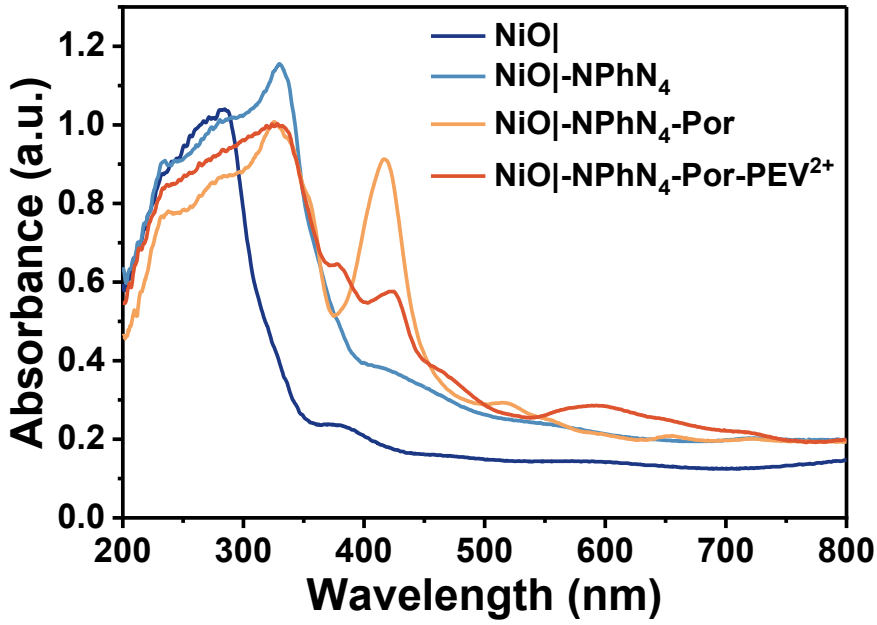

Fig. S11 Solid-state UV−vis spectra of NiO|, NiO|–NPhN$_4$, NiO|–NPhN$_4$–Por, and NiO|–NPhN$_4$–Por–PEV^{2+}.

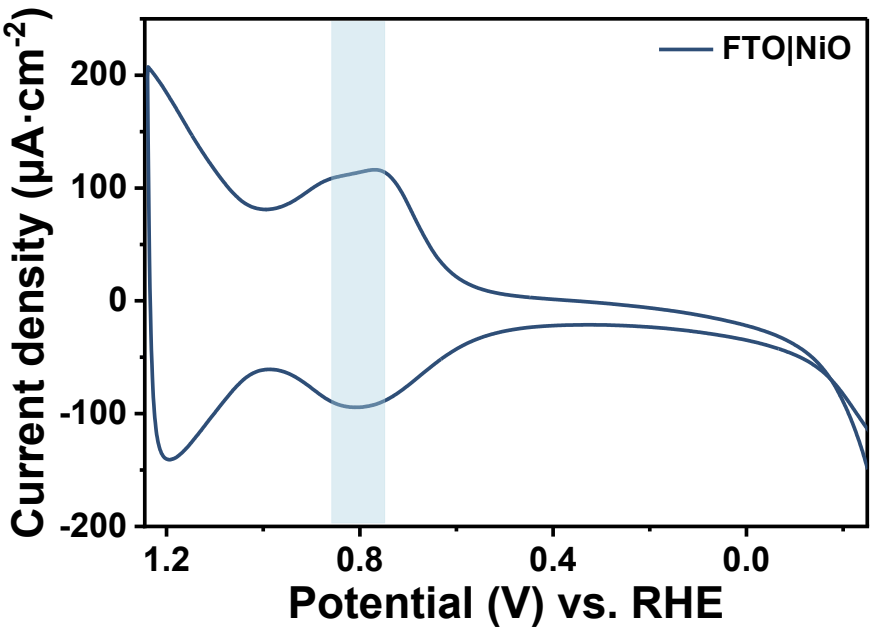

Fig. S12 Cyclic voltammograms (CVs) of FTO|NiO electrodes in 0.1 M acetic acid/acetate buffer at pH 5.8 in 0.5 M $NaClO_4$.

The 0.8 V vs RHE value for the NiO valence band edge refers to electrochemical value from the onset of the $Ni^{III}OH/Ni^{II}OH_2$ redox feature, which is likely close to (200 mV more anodic) the true valence band edge of NiO measured on an ALD-coated electrode.[5]

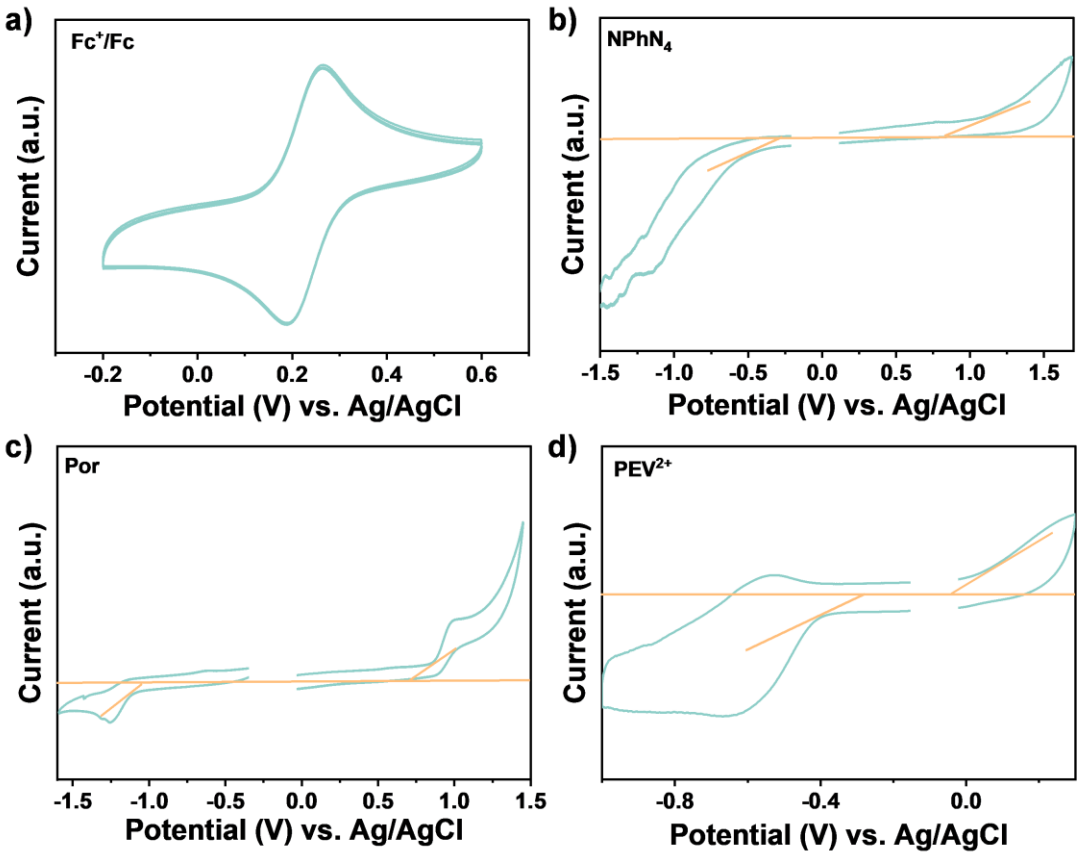

Fig. S13 CV of a) Fc^{+}/Fc, b) $NPhN_4$, c) Por and d) PEV^{2+} measured in 0.1 $mol \cdot L^{-1}$ Bu_4NPF_6 acetonitrile solution.

The HOMO and LUMO energy levels of organic semiconductors were determined by CV.[6-9] Measurements were performed in a three-electrode system with 0.1 $mol \cdot L^{-1}$ Bu_4NPF_6 in acetonitrile as the supporting electrolyte, using a working electrode modified with a thin film of the sample under anhydrous and oxygen-free inert atmosphere. The onset oxidation potential (φ_{ox}) was measured by scanning positively from 0 V, and the onset reduction potential (φ_{red}) was measured by scanning negatively from 0 V. The half-wave potential of the internal standard ferrocene $\varphi(Fc^{+}/Fc)$ was recorded under identical conditions. (Redox potential of Fc^{+}/Fc is 0.23 V vs. Ag/AgCl in our measurement system) Accordingly, the HOMO energy level corresponds to the onset oxidation potential and the LUMO energy level corresponds to the onset reduction potential. The absolute energy levels relative to the vacuum level were calculated using the Eq. 5-6:

$$E_{HOMO} = -e(\varphi_{ox} - \varphi(Fc^+/Fc) + 4.8)\ eV \quad \text{(Eq. 5)}$$

$$E_{LOMO} = -(\varphi_{red} - \varphi(Fc^+/Fc) + 4.8)\ eV \quad \text{(Eq. 6)}$$

The HOMO and LUMO energy levels (vs. Vacuum) were converted to the normal hydrogen electrode (NHE) scale using the Eq. 7:

$$E_{vs.\ NHE}\ (V) = -E_{vs.\ Vac}\ (eV) - 4.5\ eV \quad \text{(Eq. 7)}$$

The band positions of the catalyst calculated by the above methods are largely consistent with those reported in previous literature.[1, 10, 11]

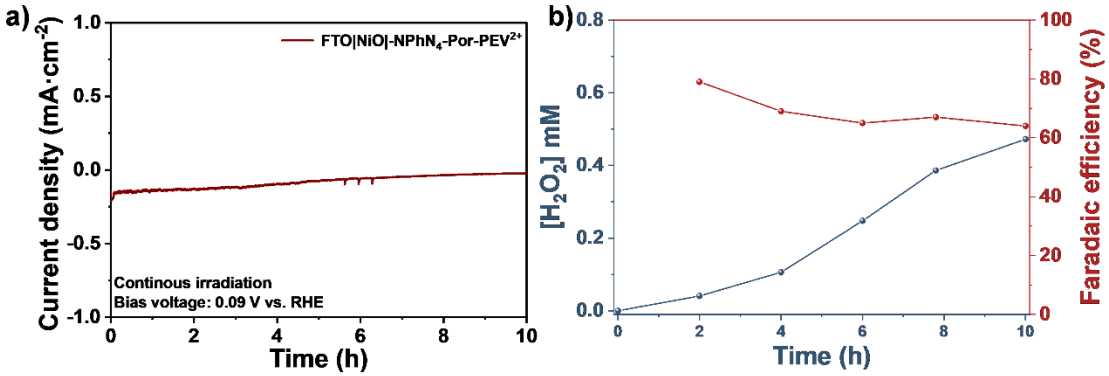

Fig. S14 The ALD-free NiO-based photocathode: a) Stability test at 0.09 V vs. RHE. b) H_2O_2 yield and Faradaic efficiency.

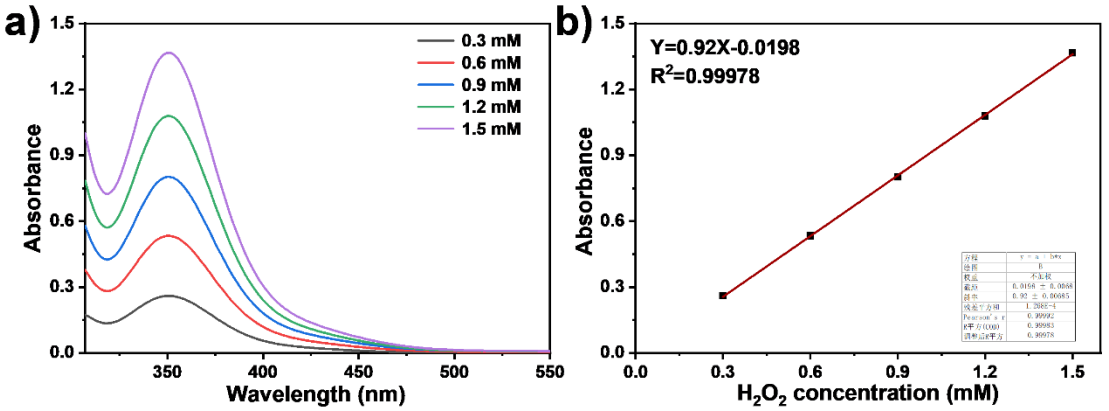

Fig. S15 a) UV-Vis absorption spectra of KI solutions with different concentrations of H_2O_2; b) Corresponding calibration curve.

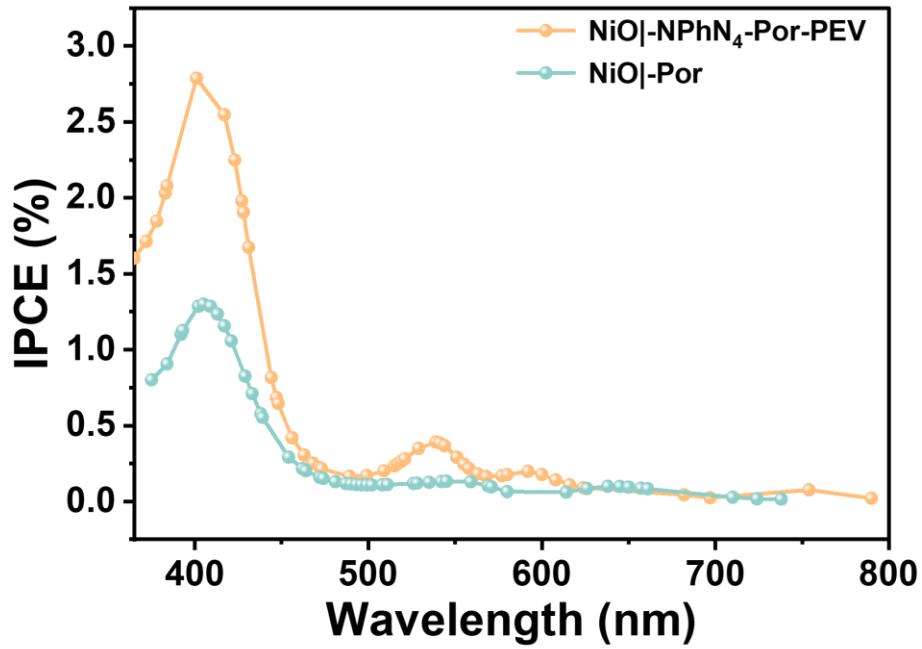

Fig. S16 IPCE of NiO|–NPhN$_4$–Por–PEV^{2+}.

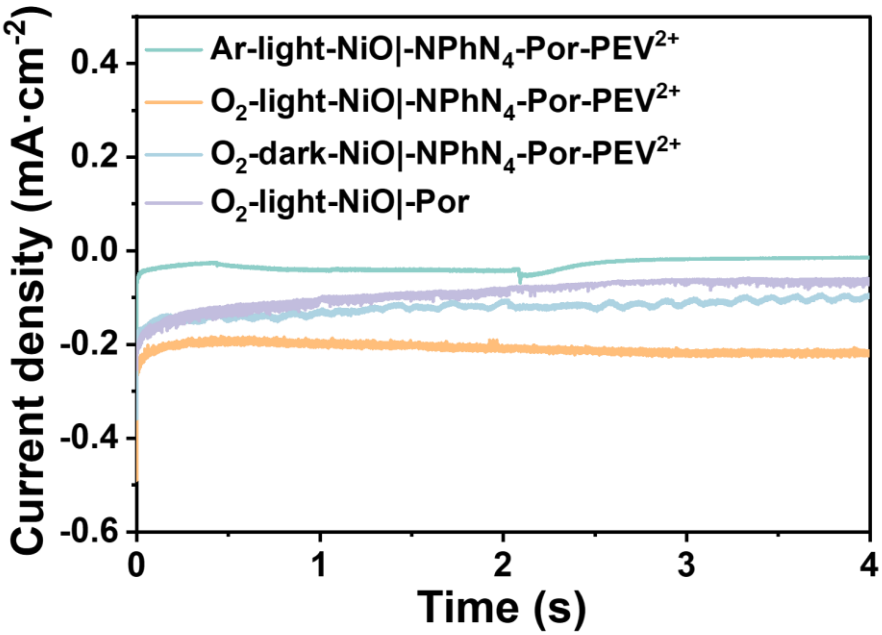

Fig. S17 Current-time curves under different conditions.

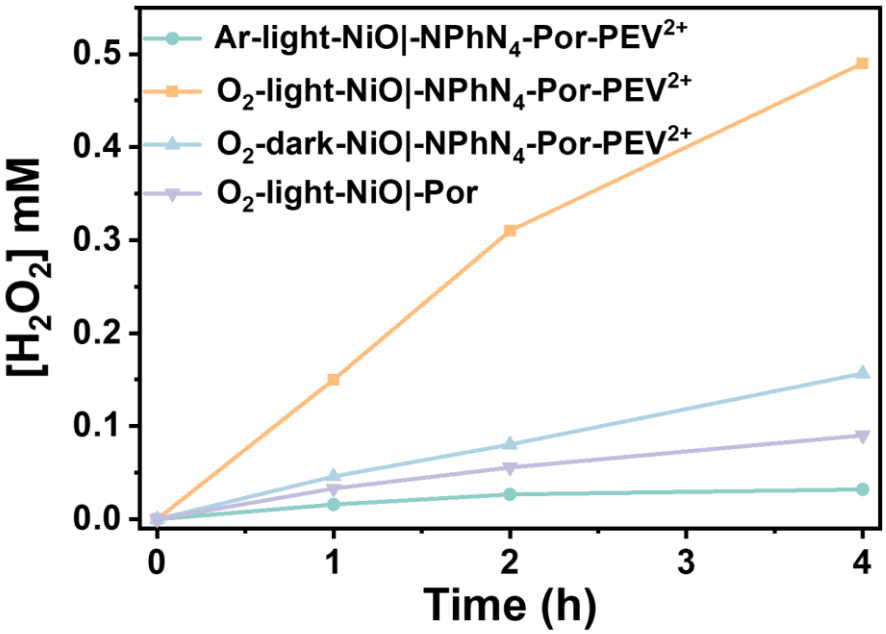

Fig. S18 H_2O_2 yield under different conditions.

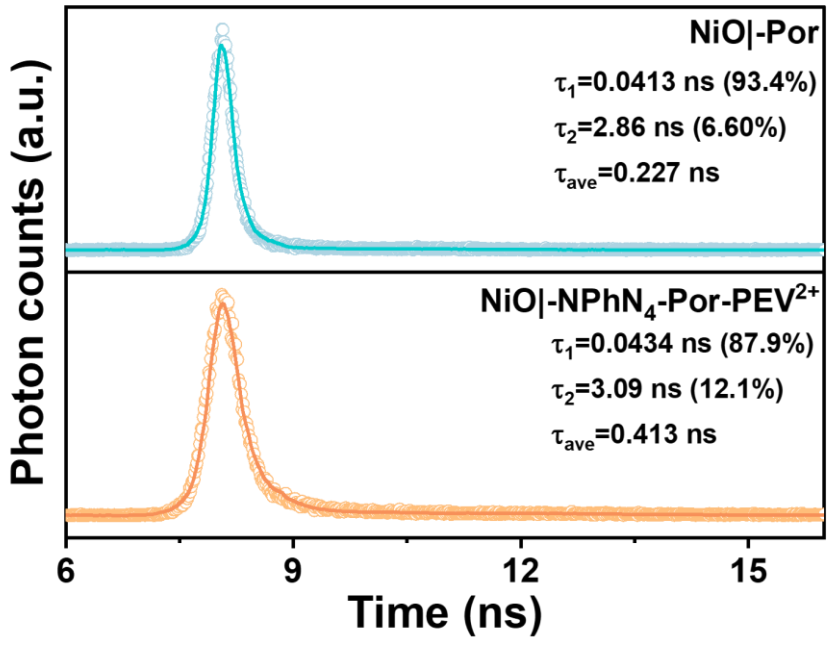

Fig. S19 Fluorescence lifetime of NiO|–Por and NiO|–$NPhN_4$–Por–PEV^{2+}.

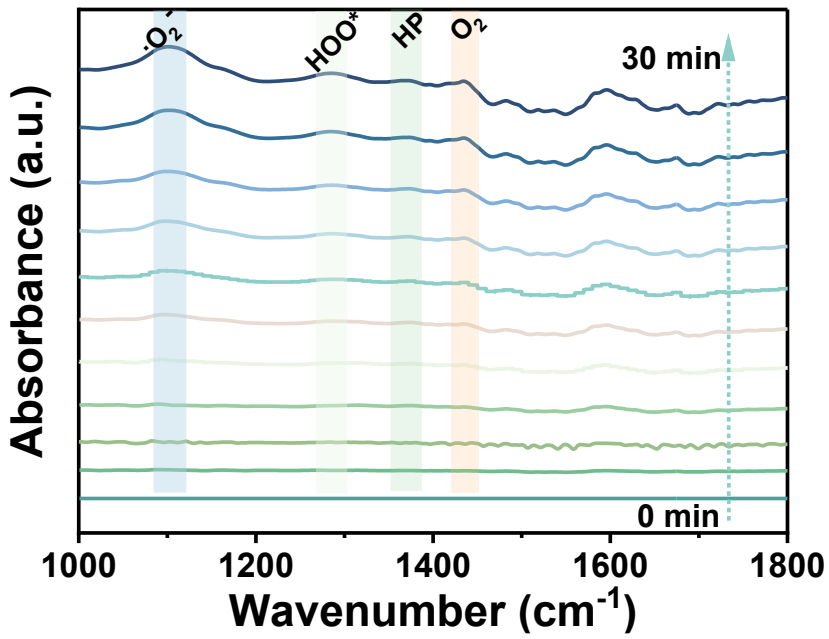

Fig. S20 *In-situ* DRIFTS spectra of NiO|–NPhN$_4$–Por–PEV^{2+} under white light irradiation in 0.09 V vs. RHE.

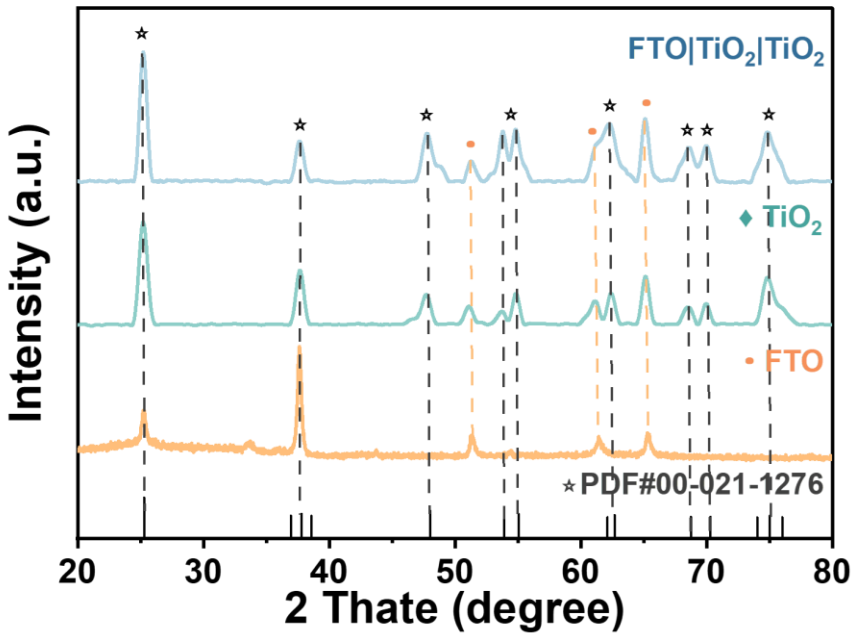

Fig. S21 PXRD patterns of FTO, TiO_2, FTO|TiO_2|TiO_2.

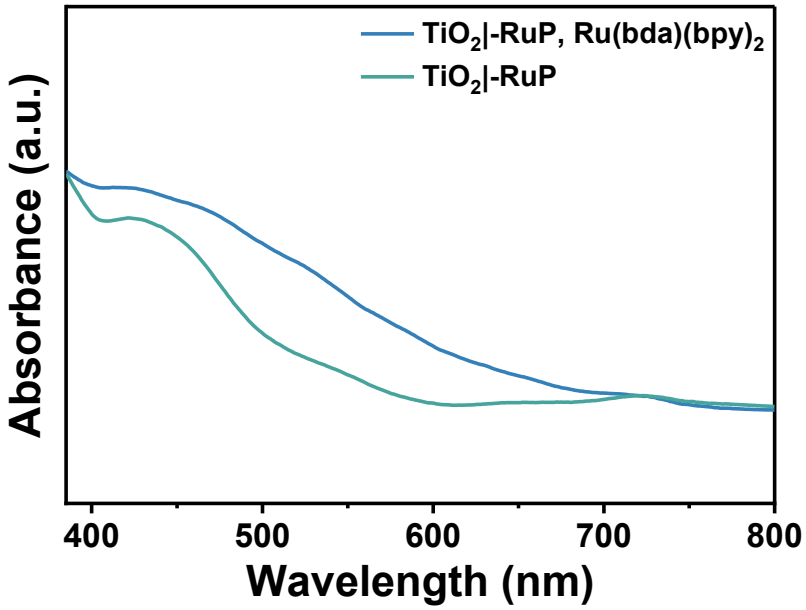

Fig. S22 UV–vis absorption of the photoanode after adsorption of the Ru(bda)(bpy)$_2$ and RuP.

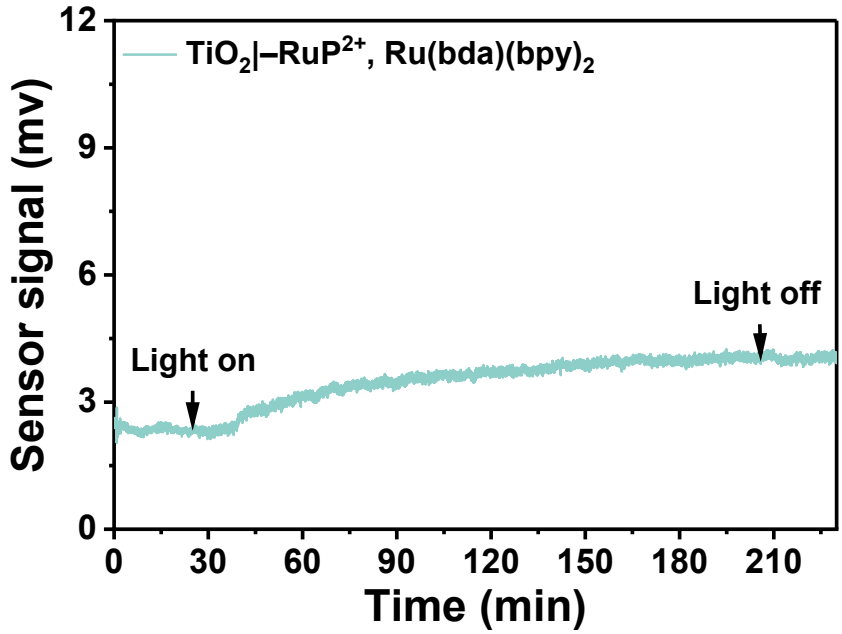

Fig. S23 Microelectrode detected oxygen sensor signal evolution of TiO_2|–RuP, Ru(bda)(bpy)$_2$ photoanode under continuous light illumination. The start and end of illumination are marked by "Light on" and "Light off", respectively.

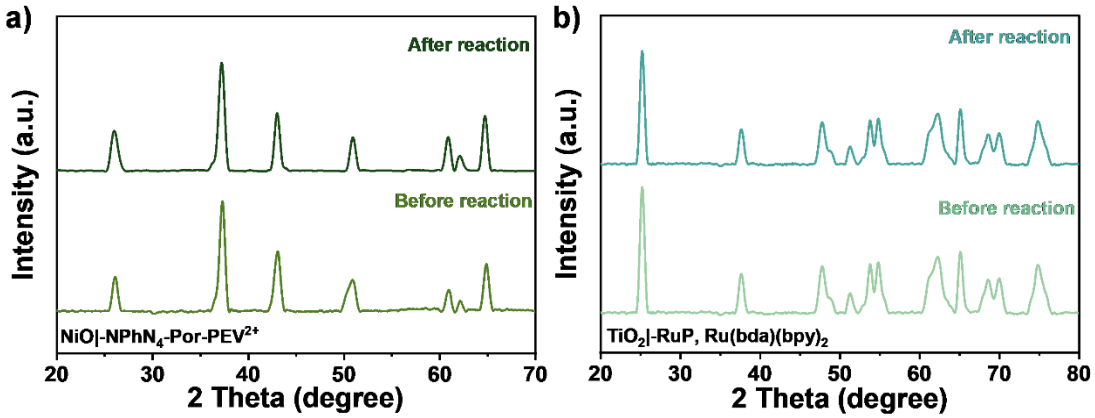

Fig. S24 PXRD patterns before and after the bias-free tandem DSPEC reaction. a) NiO|–$NPhN_4$–Por–PEV^{2+}. b) TiO_2|–RuP, $Ru(bda)(bpy)_2$.

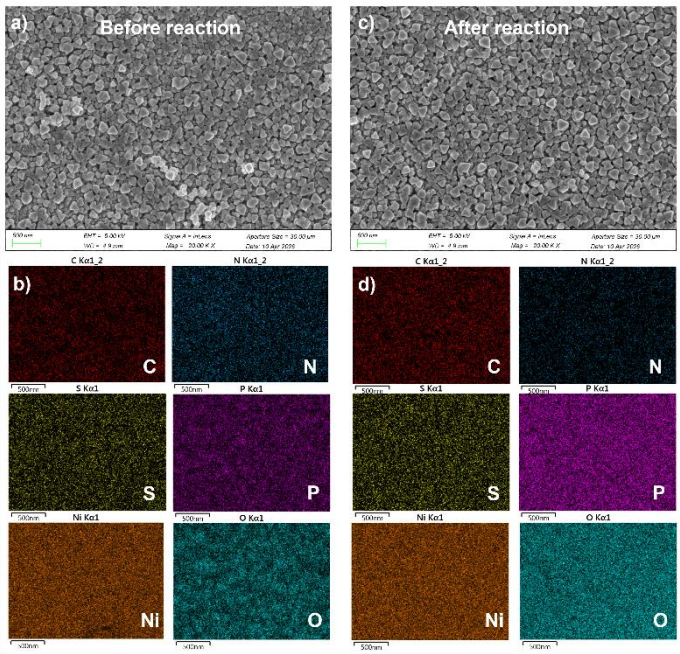

Fig. S25 SEM images and EDS elemental mappings of NiO|–$NPhN_4$–Por–PEV^{2+} before and after the bias-free tandem DSPEC reaction. a) SEM before reaction. b) EDS mapping before reaction. c) SEM after reaction. d) EDS mapping after reaction.

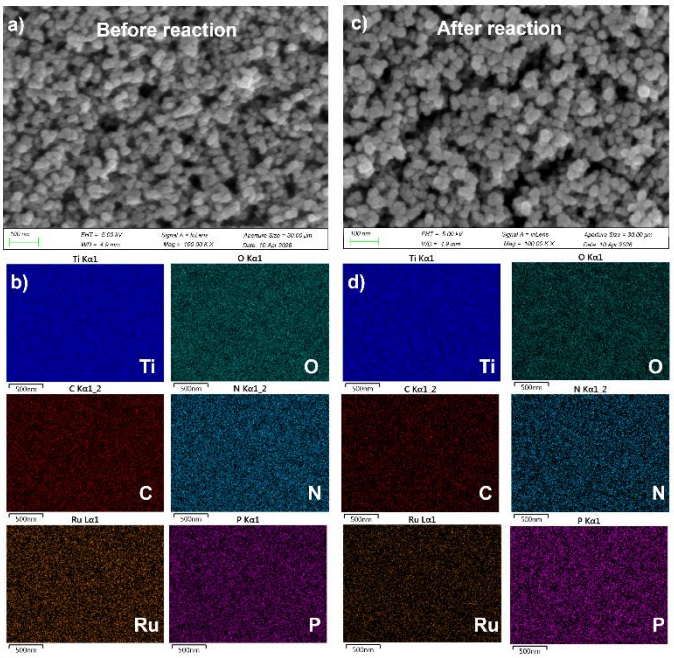

Fig. S26 SEM images and EDS elemental mappings of TiO_2|–RuP, $Ru(bda)(bpy)_2$ before and after the bias-free tandem DSPEC reaction. a) SEM before reaction. b) EDS mapping before reaction. c) SEM after reaction. d) EDS mapping after reaction.

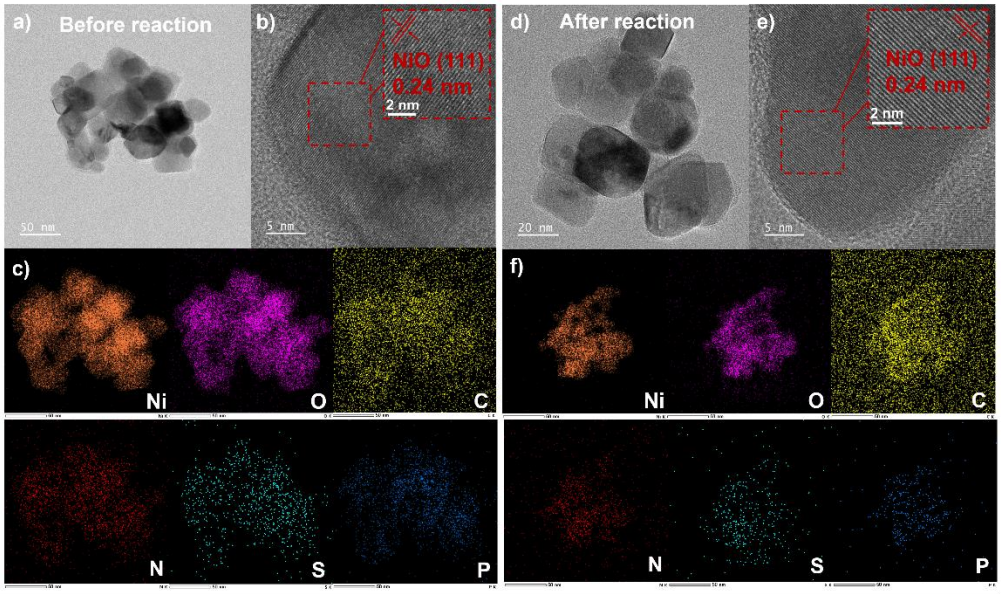

Fig. S27 TEM images and EDS elemental mappings of NiO|–$NPhN_4$–Por–PEV^{2+} before and after the bias-free tandem DSPEC reaction. a-b) TEM and c) EDS mapping before reaction. d-e) TEM and f) EDS mapping after reaction.

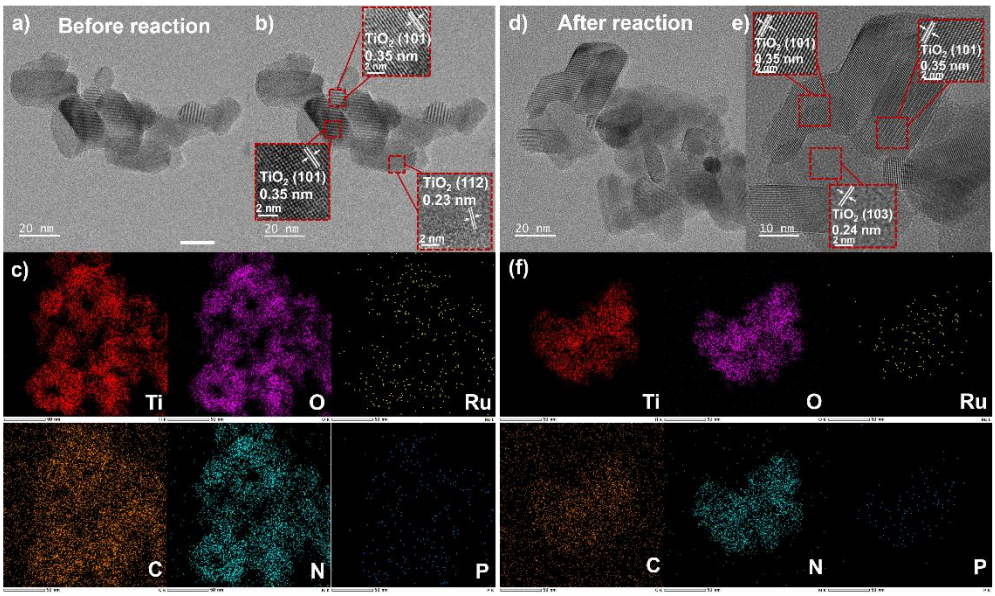

Fig. S28 TEM images and EDS elemental mappings of TiO_2|–RuP, $Ru(bda)(bpy)_2$ before and after the bias-free tandem DSPEC reaction. a-b) TEM and c) EDS mapping before reaction. d-e) TEM and f) EDS mapping after reaction.

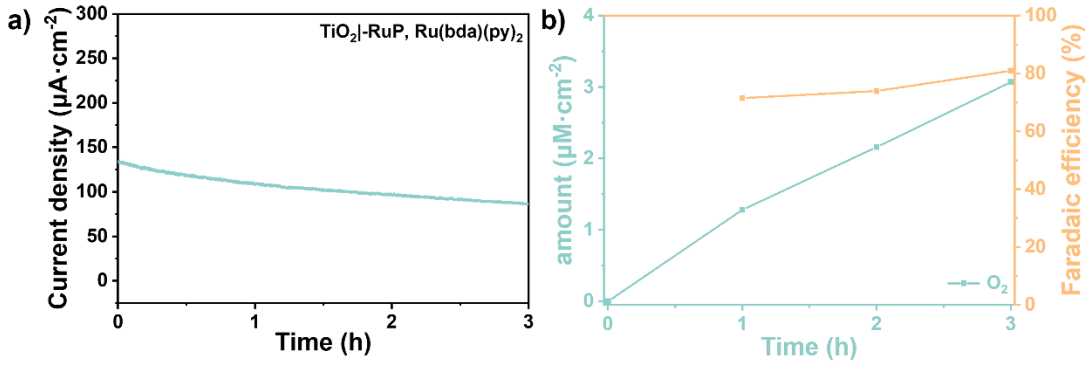

Fig. S29 a) Stability test at 1.14 V vs. RHE. b) O_2 yield and Faradaic efficiency at 1.14 V vs. RHE in 0.1 M acetic acid/acetate buffer at pH 5.8 in 0.5 M $NaClO_4$.

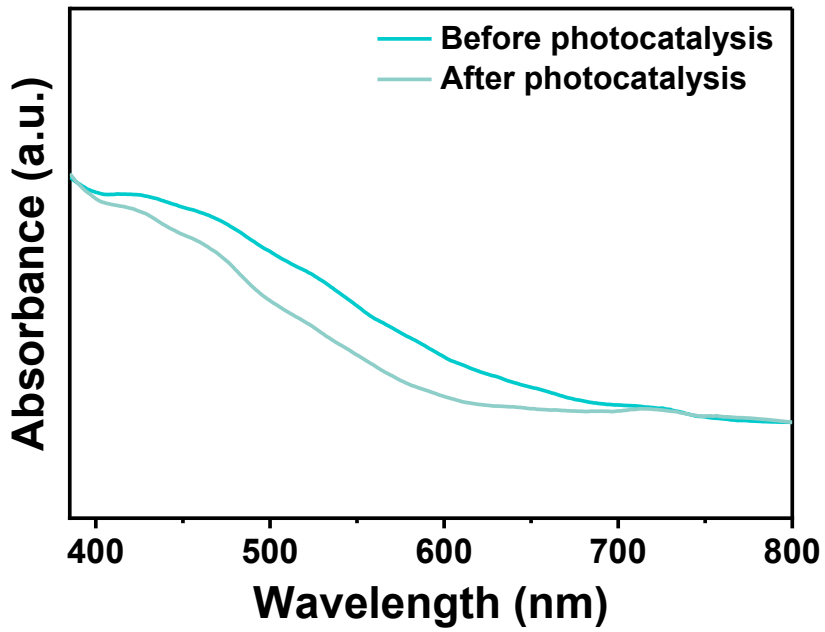

Fig. S30 UV-visible spectra of TiO_2|–RuP, Ru(bda)$(bpy)_2$ before and after photocatalysis.

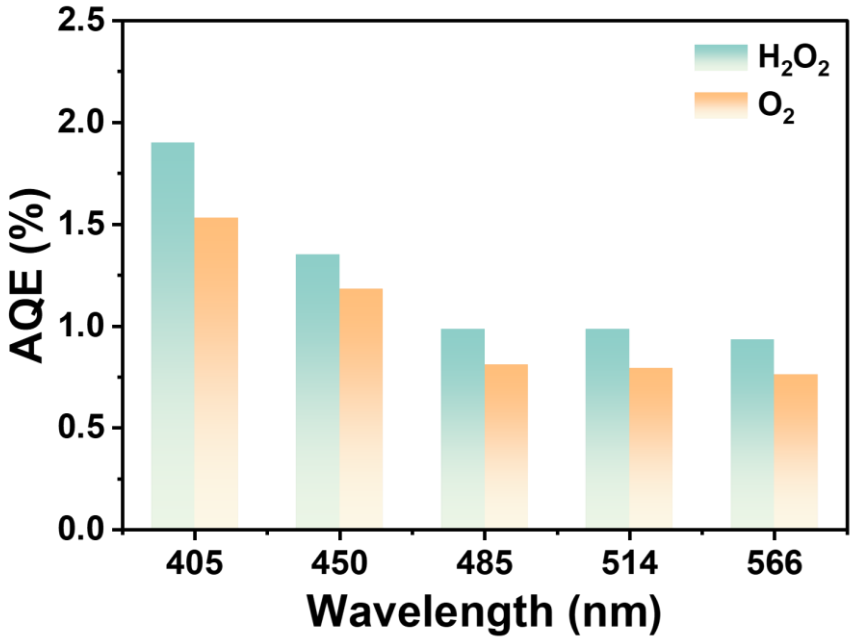

Fig. S31 AQY values for H_2O_2 and O_2 production at various wavelengths in a bias-free tandem DSPEC.

Table. S1 Performance of NiO-based photocathodes.

Sensitizer	Catalyst	Applied potential (electrolyte Ph)	Photocurrent density (illumination time)	product	FE %	Ref.
Por	$NPhN_4$-PEV^{2+}	0.09 *vs* RHE (pH 5.8)	200 μA·cm^{-2} (10 h)	H_2O_2	95.5	This work
BH4	–	0.22 V *vs* RHE (pH 6.0)	200 μA·cm^{-2} (24 h)	H_2O_2	60	12
Por	–	0.55 V *vs* RHE (pH 6.0)	50 μA·cm^{-2} (24 h)	H_2O_2	10 0± 10	10
Ru^{II}	Ni^{II}	-0.25 V *vs* NHE (pH 5.0)	20 μA·cm^{-2} (2 h)	H_2	86	13
pRK1	$1(BF_4)_2$	0.07 V *vs* RHE (pH 4.5)	20 μA·cm^{-2} (6 h)	H_2	66	14
RBG-174	Co_{C11P}	0.14 V *vs* RHE (pH 5.5)	8 μA·cm^{-2} (2 h)	H_2	65	15
Ru^{II}	Re^{I}	-0.7 V *vs* Ag/AgCl (pH 4.5)	25 μA·cm^{-2} (10 h)	CO	65	16
YB6	–	0.39 V *vs* RHE (pH 6.5)	300 μA·cm^{-2} (5 h)	H_2O_2	–	17

PB6	–	0.39 V *vs* RHE (pH 6.5)	252 μA·cm^{-2} (5 h)	H_2O_2	–	17
D-Cu(I)-A	–	-0.4 V *vs* Ag (pH 7)	8.2 μA·cm^{-2} (300 s)		–	18
P1	Co1	-0.2 V *vs* Ag/AgCl (pH 7)	35 μA·cm^{-2} (90 min)	H_2	68	19

Copies of NMR spectra

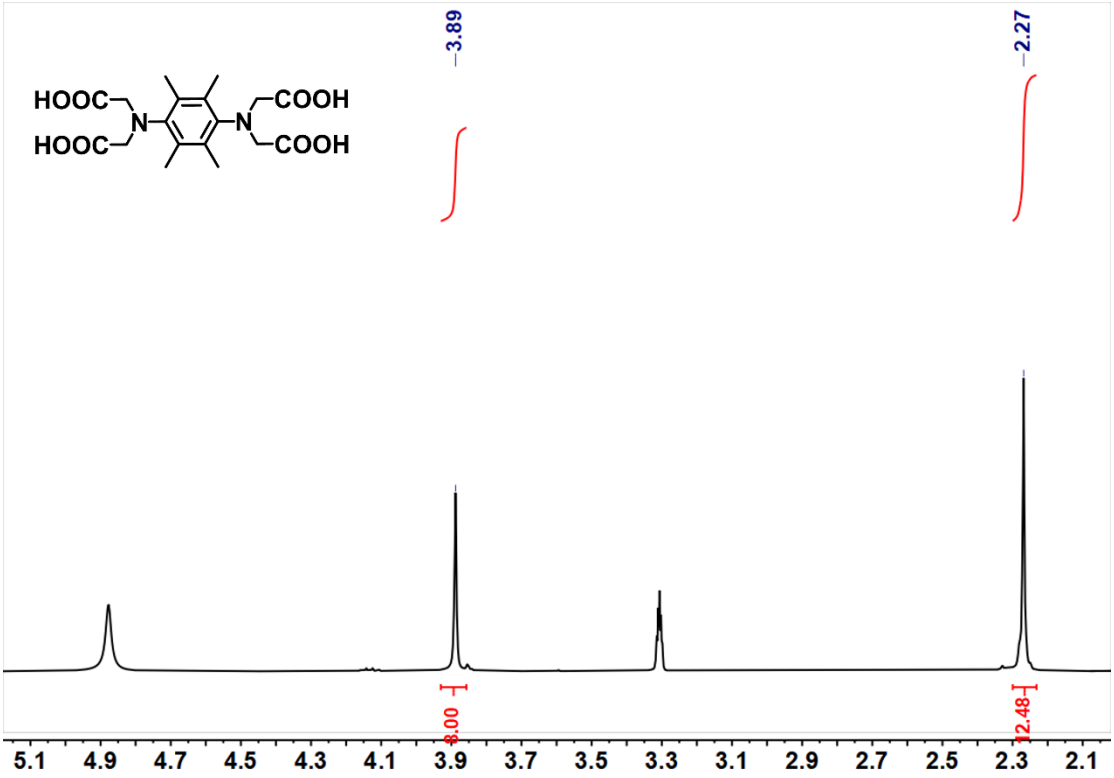

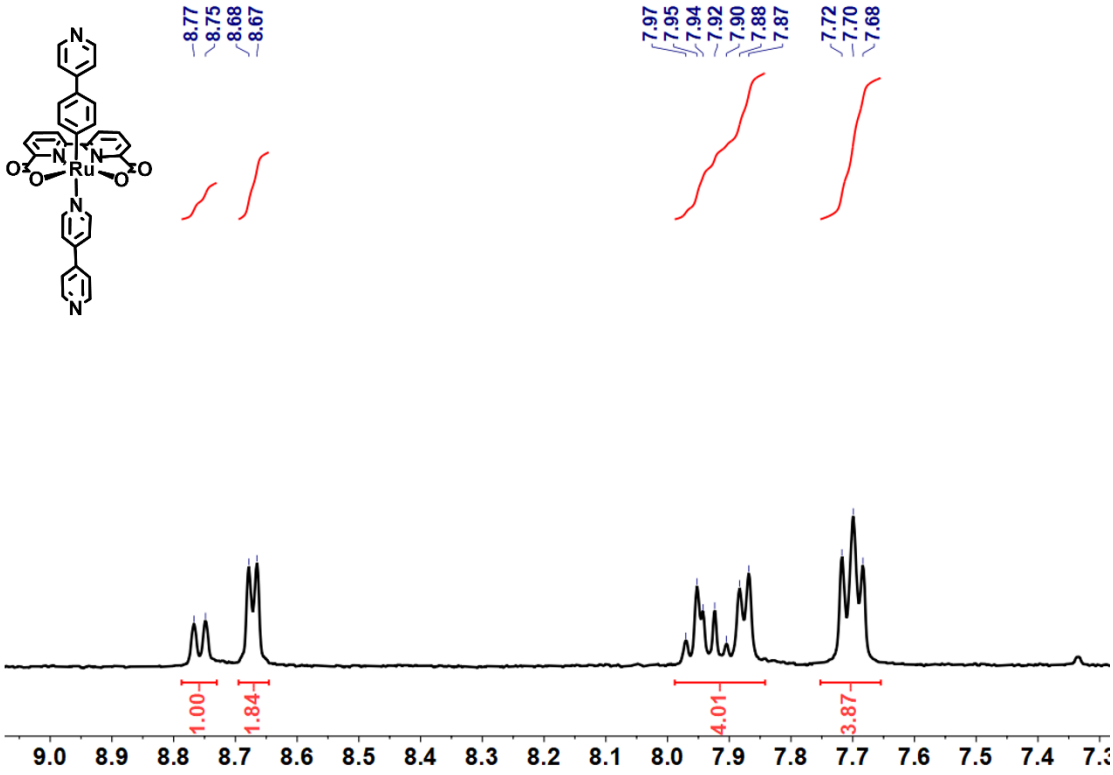

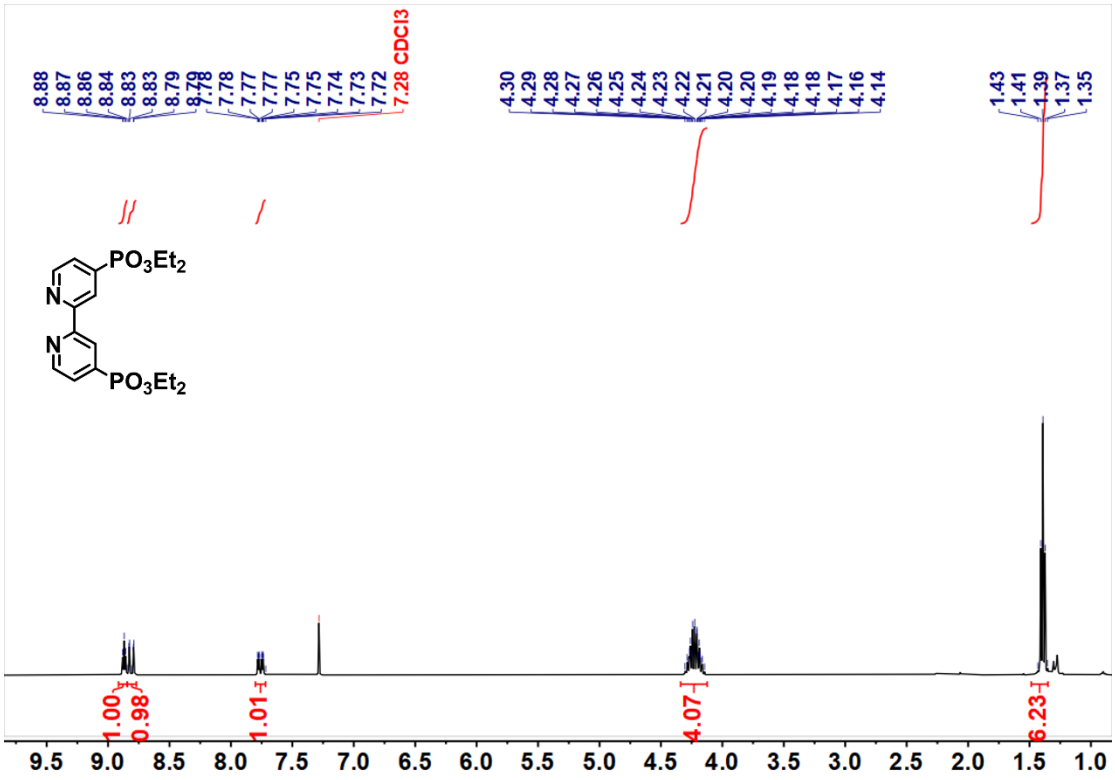
8.88
8.87
8.86
8.84
8.83
8.83
8.79
7.78
7.78
7.77
7.77
7.75
7.75
7.74
7.73
7.72
7.28 CDCl3
4.30
4.29
4.28
4.27
4.26
4.25
4.24
4.23
4.22
4.21
4.20
4.20
4.19
4.18
4.18
4.17
4.16
4.14
1.43
1.41
1.39
1.37
1.35
PO3Et2
PO3Et2
1.00
0.98
1.01
4.07
6.23
9.5 9.0 8.5 8.0 7.5 7.0 6.5 6.0 5.5 5.0 4.5 4.0 3.5 3.0 2.5 2.0 1.5 1.0

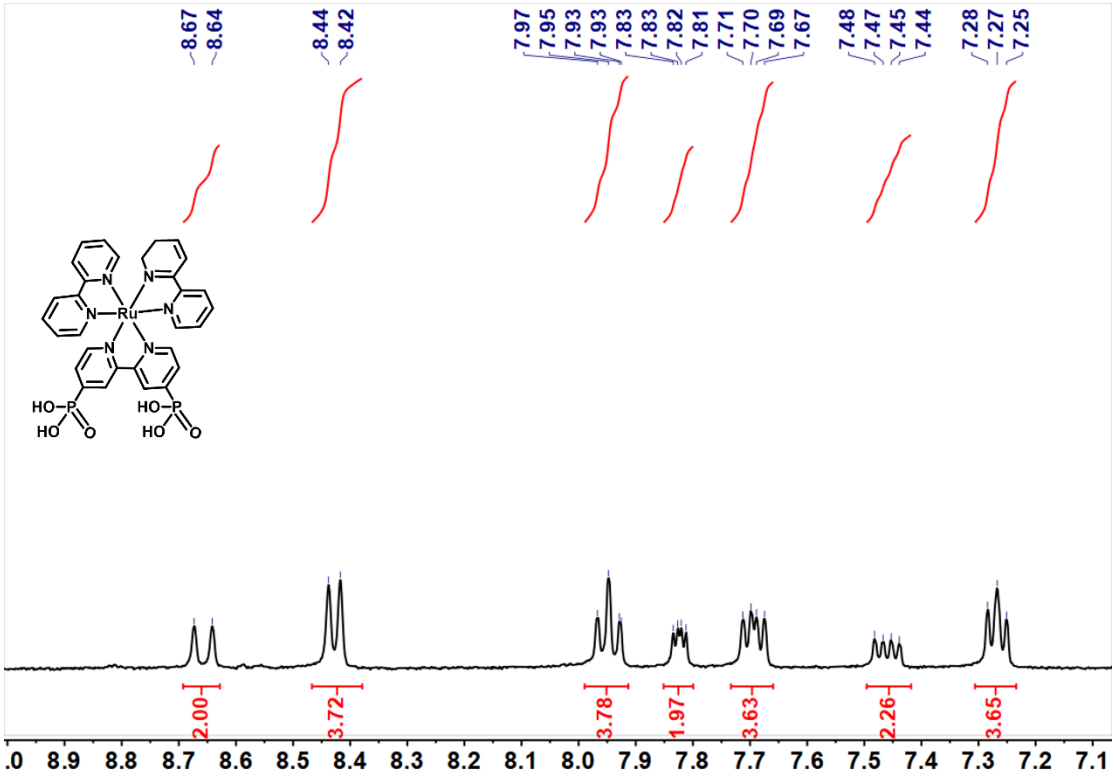
8.67
8.64
8.44
8.42
7.97
7.95
7.93
7.93
7.83
7.83
7.82
7.81
7.71
7.70
7.69
7.67
7.48
7.47
7.45
7.44
7.28
7.27
7.25
Ru
HO-P
HO
O
2.00
3.72
3.78
1.97
3.63
2.26
3.65
.0 8.9 8.8 8.7 8.6 8.5 8.4 8.3 8.2 8.1 8.0 7.9 7.8 7.7 7.6 7.5 7.4 7.3 7.2 7.1

Supplementary References

1. B. Shan, S. Vanka, T.-T. Li, L. Troian-Gautier, M. K. Brennaman, Z. Mi and T. J. Meyer, Nat. Energy, 2019, **4**, 290-299.
2. R. A. Luna-Ixmatlahua, A. Carrasco-Ruiz, R. Cervantes, A. Vela and J. Tiburcio, Chem. – Eur. J., 2019, **25**, 14042-14047.
3. Y. Zhu, D. Wang, Q. Huang, J. Du, L. Sun, F. Li and T. J. Meyer, Nat. Commun., 2020, **11**, 4610.
4. M. R. Norris, J. J. Concepcion, C. R. K. Glasson, Z. Fang, A. M. Lapides, D. L. Ashford, J. L. Templeton and T. J. Meyer, Inorg. Chem., 2013, **52**, 12492-12501.
5. C. J. Flynn, S. M. McCullough, E. Oh, L. Li, C. C. Mercado, B. H. Farnum, W. Li, C. L. Donley, W. You, A. J. Nozik, J. R. McBride, T. J. Meyer, Y. Kanai and J. F. Cahoon, ACS Appl. Mater. Interfaces, 2016, **8**, 4754-4761.
6. C. Sun, F. Pan, H. Bin, J. Zhang, L. Xue, B. Qiu, Z. Wei, Z.-G. Zhang and Y. Li, Nat. Commun., 2018, **9**, 743.
7. X. Li, R. Ma, T. Liu, Y. Xiao, G. Chai, X. Lu, H. Yan and Y. Li, Sci. China Chem., 2020, **63**, 1256-1261.
8. X. Li, S. Luo, H. Sun, H. H.-Y. Sung, H. Yu, T. Liu, Y. Xiao, F. Bai, M. Pan, X. Lu, I. D. Williams, X. Guo, Y. Li and H. Yan, Energy Environ. Sci., 2021, **14**, 4555-4563.
9. C. M. Cardona, W. Li, A. E. Kaifer, D. Stockdale and G. C. Bazan, Adv. Mater., 2011, **23**, 2367-2371.
10. O. Jung, M. L. Pegis, Z. Wang, G. Banerjee, C. T. Nemes, W. L. Hoffeditz, J. T. Hupp, C. A. Schmuttenmaer, G. W. Brudvig and J. M. Mayer, J. Am. Chem. Soc., 2018, **140**, 4079-4084.
11. B. H. Farnum, K.-R. Wee and T. J. Meyer, Nat. Chem., 2016, **8**, 845-852.
12. J. Sun, Y. Yu, A. E. Curtze, X. Liang and Y. Wu, Chem. Sci., 2019, **10**, 5519-5527.
13. B. Shan, B. D. Sherman, C. M. Klug, A. Nayak, S. L. Marquard, Q. Liu, R. M. Bullock and T. J. Meyer, J. Phys. Chem. Lett., 2017, **8**, 4374-4379.
14. C. Bourguignon, A. Moinel, A. Huet, Y. Kervella, C. D. Windle, J. Massin, V. Artero, M. Chavarot-Kerlidou and R. Demadrille, Adv. Energy Sustain. Res., 2023, **4**, 2300095.
15. N. Kaeffer, C. D. Windle, R. Brisse, C. Gablin, D. Leonard, B. Jousselme, M. Chavarot-Kerlidou and V. Artero, Chem. Sci., 2018, **9**, 6721-6738.
16. T.-T. Li, B. Shan and T. J. Meyer, ACS Energy Lett., 2019, **4**, 629-636.
17. B. Cai, S. Wrede, S. Wang, L. Kloo, G. Boschloo and H. Tian, ChemPhotoChem, 2024, **8**, e202300297.
18. Z. Singh, J. D. Chiong, J. F. Ricardo-Noordberg, S. Kamal and M. B. Majewski, Dalton Trans., 2024, **53**, 18923-18931.
19. F. Li, K. Fan, B. Xu, E. Gabrielsson, Q. Daniel, L. Li and L. Sun, J. Am. Chem. Soc., 2015, **137**, 9153-9159.